Journal of Materials Chemistry C

Dual-mode Surface-Enhanced Raman Scattering Sensors Assembled from Graphene Plasmonic Nanoresonator on Photoactive SOI

Journal:	*Journal of Materials Chemistry C*
Manuscript ID	TC-ART-05-2022-001880.R1
Article Type:	Paper
Date Submitted by the Author:	11-Jul-2022
Complete List of Authors:	Zhang, Shan; Ningbo University, Department of Microelectronic Science and Engineering, School of Physical Science and Technology Zhang, Guanglin; Ningbo University, Department of Microelectronic Science and Engineering, School of Physical Science and Technology Liu, Zhiduo; Beijing Institute of Technology, School of Physics He, Zhengyi; Ningbo University Feng, Xiaoqiang; Ningbo University Yang, Siwei; Shanghai Institute of Microsystem and Information Technology, Chinese Academy of Science, State Key Laboratory of Functional Materials for Informatics Ding, Guqiao; Shanghai Institute of Microsystem and Information Technology Chinese Academy of Sciences, Wang, Gang; Ningbo University, Department of Microelectronic Science and Engineering, School of Physical Science and Technology Wang, Yongqiang; Los Alamos National Laboratory,

Dual-mode Surface-Enhanced Raman Scattering Sensors Assembled from Graphene Plasmonic Nanoresonator on Photoactive SOI

Shan Zhang[1], Guanglin Zhang[1], Zhiduo Liu[2], Zhengyi He[1], Xiaoqiang Feng[1], Siwei Yang[3], Guqiao Ding[1,3], Gang Wang[1,*] and Yongqiang Wang[4,*]

[1]Department of Microelectronic Science and Engineering, School of Physical Science and Technology, Ningbo University, Ningbo 315211, P. R. China.

[2]Centre for Quantum Physics, Key Laboratory of Advanced Optoelectronic Quantum Architecture and Measurement (MOE), School of Physics, Beijing Institute of Technology, Beijing 100081, P. R. China.

[3]State Key Laboratory of Functional Materials for Informatics, Shanghai Institute of Microsystem and Information Technology, Chinese Academy of Sciences, Shanghai 200050, P. R. China.

[4]Materials Science and Technology Division, Los Alamos National Laboratory, Los Alamos, New Mexico 87545, USA.

*Correspondence to: gangwang@nbu.edu.cn (G. Wang); yqwang@lanl.gov (Y. Wang)

Abstract

Surface-enhanced Raman scattering (SERS) has been explored and acts as a practical analytical detection approach. However, constructing highly sensitive SERS substrates usually involves expensive materials and tedious preparation processes, and SERS substrates often cannot be reused. Herein, direct hetero-integration of three-dimensional graphene (3D-graphene) with silicon-on-insulator (SOI) substrate can be utilized as a highly stable, ultra-sensitive, low cost and reusable SERS substrates through plasma-assisted chemical vapor deposition (PACVD). The novel nanocavity construction of the 3D-graphene combines with the optical cavity system of the SOI to improve the interaction between the incident light and 3D-graphene, which is a model for doubly-reinforced Raman scattering. These properties enhance electronic interactions between 3D-graphene, target molecules, and SOI substrates, thereon improving chemical/charge transfer effects in heterojunctions. The as-designed 3D-graphene/SOI heterojunction has detection limits of ~10^{-10} M for rhodamine B (RB) and rhodamine 6G (R6G), and detection limits for crystalline violet (CRV) is ~10^{-8} M, which is better than the existing reported graphene-based SERS. Our study confirms the efficient carrier transfer mechanism in the 3D-graphene/SOI heterojunction and enhances the chemical/charge transfer mechanism of SERS by double-enhanced high-light absorption. In addition, erythrosine B (EB) and carmine, considered a harmful pigment additive in fruit-flavored beverages, were selected as the detection target with a detection limit of about 10^{-9} M and 10^{-8} M, suggesting that 3D-graphene/SOI heterojunction-based SERS can be applied in the food safety field.

Keywords: SERS, 3D-graphene, Reusable, Chemical/charge transfer, Food safety

1. Introduction

SERS technology has been widely employed in biological sensing, drug resolution, environmental monitoring, and food safety detection.[1-5] It mainly relies on two mechanisms, namely the electromagnetic mechanism (EM) and chemical mechanism (CM)[6-10]: (i) EM is mainly derived from noble metal nanoparticles, such as gold and silver etc.;[13] and (ii) CM arises from the interaction between nanostructures and the electronic levels of the target.[11,12]

However, the cost of preparing these SERS substrates is very high due to the many complex and uncontrollable processes involved.[14] Noted that due to the active chemical properties of noble metal, the SERS substrate of this kind has poor stability and often cannot be reused.[15] Thus, to meet the needs of practical applications, it is required to explore new Raman-enhanced substrates. Recently, two-dimensional (2D) graphene films and their derivatives have been used as noble metal-free SERS substrates. The special SERS effect is mainly derived from the CM established on its outstanding optical and electrical features.[16-22] Compared with noble metals, graphene-based materials have the advantages of chemical stability and low cost.[23-26] Unfortunately, the weak ability to absorb light (only 2.3%) of a 2D-graphene monolayer means light interacts poorly with the matter, limiting its performance in practical Raman enhancement applications.[27]

3D-graphene is a natural graphene plasmonic nano-resonator arranged vertically growing on a target substrate. It combines many unique characteristics of 2D-graphene (chemical inertness, specific surface area and high electrical conductivity)[28-32] and

possesses different properties from planar graphene owing to the special 3D structure. The large specific surface area of 3D-graphene is attributed to its porous structure, providing more prominent adsorption sites for target molecules. At the same time, many exposed edges of atomic levels lead to a high electroactive surface area and thus fast electron transport dynamics.[33] Based on the porous structure of 3D-graphene, the interaction of incident light and 3D-graphene can be substantially stronger than planar graphene.[34] These special features suggest that 3D-graphene could be suitable for designing high-performance SERS substrates.

SOI is a substrate technology that replaces the traditional bulk substrate silicon with an "engineered" substrate formed by three layers: a nanoscale top layer of monocrystalline silicon, a relatively thin interlayer of insulating silicon dioxide and a very thick layer of the bulk silicon substrate.[35-37] The unique resonator construction of the SOI substrate can serve as a bottom reflector in the 3D-graphene/SOI heterojunction, which means that a multi-channel reflection strategy can recover light that the 3D-graphene has not absorbed.

This work depicts highly stable, ultra-sensitive, low-cost and reusable SERS substrates to synthesize 3D-graphene/SOI heterojunctions based on PACVD. PACVD is a low-temperature, easily scalable, and inexpensive method for directly preparing 3D-graphene with clean surfaces and interfaces on arbitrary substrates. Furthermore, the nanocavity structure of 3D-graphene integrated with the optical cavity structure of the SOI dramatically enhances the interaction between incident light and 3D-graphene,

thus resulting in markedly improved light detection sensitivity of 3D-graphene/SOI heterojunctions surface.

The 3D-graphene/SOI heterojunction arrays acted as SERS substrates for detecting three probe molecules: R6G, RB, and CRV. The experimental results indicate that our novel SERS substrate is ultra-sensitive to different molecules: the lowest detection limits of the 532 nm laser for R6G, RB, and CRV were determined to be approximately 10^{-10}, 10^{-10} and 10^{-8}, respectively. In addition, washing these SERS substrates with ethyl alcohol can effectively remove the adsorbed molecules and enable their reuse. Furthermore, the 3D-graphene/SOI heterojunction SERS substrates are highly uniform in SERS performance with relative standard deviations (RSDs) of ~4% for a size 10 × 10 mm^2 sensing area. In addition, the as-designed 3D-graphene/SOI heterojunction can detect the harmful pigment additive EB and carmine in fruit-flavored beverages with high sensitivity with a detection limit of about 10^{-9} M and 10^{-8} M. All these performance characteristics shows an excellent potential to open a new avenue for applying this improved SERS technique in biosensing, drug analysis, food safety detection and other emerging fields.

2. Experimental Section

2.1 Probe molecular materials

R6G, RB, CRV, EB and carmine were purchased from Aladdin Reagents (Shanghai, China Co., Ltd.) as dye probe molecules. The test concentrations for both R6G and RB were diluted to 10^{-10}–10^{-4} M, while CRV was diluted to 10^{-8}–10^{-4} M, EB

was diluted to 10^{-9}–10^{-4} M, and carmine was diluted to 10^{-8}–10^{-4} M.

2.2 Fabrication of 3D-graphene/SOI

3D-graphene growth was achieved *via* the low-temperature PACVD technology. Put the SOI substrate into the target position of the chamber, first vacuum the chamber to about 5 Pa, then add 1 sccm hydrogen (H_2) and 10 sccm argon (Ar) mixed gas flow before heating the PACVD temperature zone system. When the temperature reaches 550 ^{o}C, turn off the H_2 and Ar, and pass through the growth gas of 10 sccm methane (CH_4). Turn on the plasma source and set its power to 200 W for 60 min growth. After the growth is finished, turn off the CH_4 gas, cool the growth chamber to room temperature by passing 10 sccm of Ar gas. Turn off the vacuum pump, wait until the chamber reaches atmospheric pressure, then turn off the Ar gas and take out the SOI samples. Similarly, the 3D-graphene growth process on other substrates of interest, such as Si and SiO_2 was done similarly.

2.3 Characterization

The surface morphology and height of the 3D-graphene/SOI were measured *via* atomic force microscopy (AFM, Oxford Instruments, Cypher S) and scanning electron microscopy (SEM, HITAGHT S-3400N). Crystallographic information of SOI and 3D-graphene were determined by transmission electron microscopy (TEM, FET-Tecnai G2F20 S-7WIN). Scanning Kelvin probe microscopy (SKPM) and conductive-AFM (C-AFM) was used to measure the potential distribution and current response of the 3D-graphene/SOI. The hydrophobicity of the 3D-graphene was measured by the

contact angle drop meter (JCA-1). The absorption spectrum was collected by ultraviolet–visible–near infrared spectroscopy (Cary 5000). Raman scattering (Jobin Yvon HR800) using a 532 nm wavelength laser was performed to evaluate the quality of the 3D-graphene structure.

2.4 SERS Measurements

Drop 5 μL of the probe solution on the SERS substrates before performing the SERS measurement, which was then allowed to dry naturally (about 10 min) for the SERS measurement. In the SERS test, a laser with a wavelength of 532 nm was operated as the excitation source, and the laser spot diameter was ~12.5 μm. The laser power was selected to 2.5 mW, and the data acquisition time was set to 10 s.

2.5 Simulation Method

The finite-element method simulations (COMSOL Multiphysics) were employed to simulate the spatial distributions of electromagnetic field intensity and power loss density of the 3D-graphene/SOI heterojunction. The incident light (532 nm) was set with an electric field (E_0=1 V/m) with X-polarization travelled along the Z-direction. The optical properties of graphene were calculated with the Lorentz-Drude model. The height of 3D-graphene is 300 nm.

3. Results and Discussion

Fig. 1(a) illustrates a schematic of a characteristic 3D-graphene structure *in-situ* grown on SOI. The cross-section TEM image indicates that the thickness of the top Si

and BOX layers of the SOI are ~150 nm and ~400 nm, respectively, as shown in **Fig. 1(b)**. A high-resolution TEM image is shown in **Fig. 1(c)** reveals the appearance of lattice fringes and the spacing between Si planes. The interplanar spacing is 3.14 Å, corresponding to Si (111) crystal planes. The inset of **Fig. 1(c)** depicts the fast Fourier transform diffraction pattern, implying the Si layer is highly crystalline (effectively a single crystal). As exhibited in **Fig. 1(d)**, the cross-sectional TEM image of a 3D-graphene/SOI heterojunction implies that the height of the 3D-graphene layer is ~300 nm thick. The 3D topography of the 3D-graphene surface, as captured using AFM, is displayed in **Fig. 1(e)**. The AFM image confirms the vertical features of the 3D structure (nanocavity), and the thickness is again ~300 nm (see also **Fig. 1(f)**), in agreement with the TEM image in **Fig. 1(d)**. **Fig. 1(g)** shows water contact angle images obtained on the 3D-graphene/SOI surface versus that on a virgin SOI. As can be obtained, the 3D-graphene is highly hydrophobic (water contact angle of 132°), mainly due to the vertical nature of the 3D structure. The porous nature of the 3D-graphene is illustrated in **Fig. 1(h)**, an estimated porosity of ~83%. The large surface area to volume ratio of the 3D-graphene/SOI surface provides more adsorption sites for target molecules. **Fig. 1(i)** compares Raman spectra obtained from a 3D-graphene/SOI SERS surface and virgin SOI substrates. The 3D-graphene produces four prominent Raman peaks: i.e., D-peak (1,349 cm^{-1}), G-peak (1,580 cm^{-1}), D′-peak (1,610 cm^{-1}), and 2D-peak (2,698 cm^{-1}). The Si component produces the other prominent peak at around 520 cm^{-1}. Note that the D and D′ peaks arise from the edge effects in the 3D-graphene structure.

The local electric field and normalized power loss density distribution were simulated using the finite-element method simulations to explore the interaction of 3D-graphene/SiO_2, 3D-graphene/Si, and 3D-graphene/SOI with light, respectively. **Figs. 2(a-c)** show the simulated local electric field distribution of the 3D-graphene on various substrates. **Fig. S1** depicts the local electric field intensity distribution along the Z-direction in **Figs. 2(a-c)** and the local electric field distribution of 3D-graphene with the optical cavity system of the SOI along the black dashed lines in **Fig. 2(c)** are extracted and shown in **Fig. 2(d).** It can be attended that the 3D-graphene/SOI heterojunction has a stronger local electric field compared to the other two substrates. Notably, the SOI substrate on which the 3D-graphene is grown significantly influences on the local electric field distribution. The local electric in the 3D-graphene and upper Si layer is very strong, indicating that 3D-graphene (nanocavity) and SOI (optical cavity) could improve the interaction between the incident light. The unique resonator construction of the SOI substrate can serve as a bottom reflector in the 3D-graphene/SOI heterojunction, which means that a multi-channel reflection strategy can recover light that the 3D-graphene has not absorbed. Moreover, the optical absorption spectra of the 3D-graphene/SOI system are presented in **Fig. 2(e)**. The results show that the optical absorption of the 3D-graphene/SOI system (blue line) is significantly higher than that of the 3D-graphene/Si (red line) and 3D-graphene/SiO_2 (black line) system, which benefits from the unique nanocavity of 3D-graphene combined with the multiple light reflection strategy of the SOI optical cavity. The interaction between 3D-graphene and incident light is improved in the 3D-graphene/SOI heterojunction. In general, the

stronger the local electric field, the stronger the absorption of incident light.[38,39] To study the influence of SOI on SERS sensitivity, by comparing SOI with its parts (e.g., Si and SiO_2), the advantages of the result of SOI are illustrated. The enhancement factor (EF) is an essential parameter of SERS sensitivity,[40-42] it can be attended that the SOI has a higher EF compared to Si and SiO_2. The relationship equation about the EF is as follows[43]: $EF \approx \left|\frac{E(\omega)}{E_0(\omega)}\right|^4$, $E_0(\omega)$ is the original electric field intensity of incident light and $E(\omega)$ is the electric field intensity excited by incident light. The specific values of $E_0(\omega)$, $E(\omega)$ and EF for SOI, Si and SiO_2 are listed in **Table S1**. The EF value of SOI is the largest. Thus, it is demonstrated that the nano-cavity structure of 3D-graphene combined with SOI greatly enhances the interaction between the incident light and 3D-graphene, resulting in a significant improvement in the light detection sensitivity of the 3D-graphene/SOI heterojunction surface. Moreover, the detection limits for these three different substrates (e. g., SOI, Si, and SiO_2) are measured, as shown in **Fig. S2**, 3D-graphene/SOI heterojunction has the highest detection limit, which can be measured to a concentration of 10^{-10} M, further indicating that the sensitivity of 3D-graphene/SOI heterojunction is the highest compared to 3D-graphene/SiO_2 and 3D-graphene/Si heterojunction. **Figs. 2(f-h)** represents the normalized power loss density distribution of the 3D-graphene/SiO_2, 3D-graphene/Si and 3D-graphene/SOI. A statistical plot of the normalized power loss density distribution along the Z-axis, as shown in **Fig. S1**, indicates that the normalized power loss density of the 3D-graphene/SOI heterojunction is the largest. The high local electric field and normalized power loss density distribution are attributed to the unique reflective structure of the SOI substrate and the

natural nano-resonant cavity of 3D-graphene, which helps to increase the intensity of light absorption.

Figs. 3(a-b) shows the measured Raman spectra from three SERS substrates: 3D-graphene/SiO_2, 3D-graphene/Si, and 3D-graphene/SOI, for detecting 10^{-6} M R6G and RB, respectively. **Fig. 3(c)** summarizes the measurement sensitivity plots for the peak intensities representing R6G and RB molecules and clearly shows that the 3D-graphene/SOI heterojunction has the best light absorption capacity and molecular adsorption efficiency of the three SERS substrates. The 3D-graphene/SOI SERS detection sensitivity was then tested for all three molecules (R6G, RB and CRV) in solutions of different concentrations through ethanol dilution, as shown in **Figs. 3(d-f)**, where the insets represent the molecular structures of R6G, RB, and CRV, respectively. These Raman spectra confirmed that the intensities of the characteristic Raman peaks in the R6G, RB and CRV spectra increased with their molecular concentrations. The minimum detection limits of these those types of molecules were determined to be 10^{-10} M for both R6G and RB, and 10^{-8} M for CRV, demonstrating the high sensitivity of the 3D-graphene/SOI substrate.

Uniformity and reproducibility of SERS substrates are critical characteristics that must be possessed in practical applications to ensure reliable detection results.[44] 3D-graphene is chemically inert and less susceptible to chemical changes, thus enabling improved repeatability and stability of 3D-graphene/SOI SERS substrates. The reproducibility and uniformity of 3D-graphene/SOI substrates were evaluated by selecting 30 random spots on the substrate of 10 mm × 10 mm, and the results are shown

in **Fig. 4(a)**. According to the Raman spectra, the intensities of the four characteristic peaks of graphene did not change significantly with the position of the spots used, indicating the super-uniformity of this SERS substrate. **Figs. 4(b-c)** presents the statistical plots of the G-peak and 2D-peak intensities, respectively, suggesting that the intensities of the 30 spots were reproducible. Based on the statistics of the primary characteristic peak intensities, the RSDs of the G-peak and 2D-peak of 3D-graphene are ~3.9 and ~4.1%, respectively. The small difference indicates the excellent uniformity and stability of the 3D-graphene/SOI SERS substrate. The stability analysis of the 3D-graphene/SOI substrate adsorbed with RB molecules (10^{-6} M) was also performed. Similarly, 30 points were randomly selected for Raman analysis, and the results are displayed in **Fig. 4(d)**. **Figs. 4(e-f)** summarize the 30 peak intensities at 1506 and 1647 cm^{-1}. The RSDs at 1506 and 1647 cm^{-1} in the Raman peak positions are ~4.7 and ~4.2%, respectively. Again, the small difference means that the designed 3D-graphene/SOI heterojunction can act as a reliable SERS substrate with a uniform SERS signal.

Target molecules adsorbed on SERS substrates based on 3D-graphene/SOI need to be easily removed to achieve the reusability of SERS substrates. We used ethanol to clean 3D-graphene/SOI substrates in our current work. Several experiments were performed to demonstrate the reusability of the SERS substrates based on 3D-graphene/SOI, as exhibited in **Fig. (5)**. **Fig. 5(a)** displays AFM images of 3D-graphene/SOI before washing and after washing cycles: no significant change in the surface morphology of 3D-graphene. In addition, the water contact angle of 3D-

graphene was almost the same before and after each cleaning, as revealed in **Fig. 5(b)**, implying that the surface structure was not noticeably changed during the ethanol washing process. Besides, we provide SERS spectra of 3D-graphene/SOI substrates before and after cleaning, as shown in **Fig. S3,** indicating that the adsorbed molecules are completely removed from the substrate after cleaning with alcohol. To demonstrate the SERS based on the 3D-graphene/SOI substrate before and after washing, 10^{-6} M R6G and RB were selected as probes, and the measured SERS spectra are depicted in **Figs. 5(c-d)**. The results showed that the characteristic peaks of R6G (i.e., 614, 774, 1364, 1511 and 1651 cm^{-1}) and their intensities are virtually the same whether the substrate was pre-washed or not, demonstrating that the SERS substrate based on 3D-graphene/SOI is highly stable and reusable.

To confirm the SERS enhancement mechanism in our 3D-graphene/SOI structure originated from CM-based charge transfer (CT),[15, 45-47] we performed combined SKPM and C-AFM characterizations. The CT values between R6G molecules and 3D-graphene/SOI were studied as an example, and the results are shown in **Fig. (6)**, demonstrating that the CT generated between 3D-graphene and SOI substrates and between 3D-graphene and R6G molecules. The surface potential distributions of 3D-graphene/SOI and R6G/3D-graphene/SOI samples were measured by SKPM and are shown in **Figs. 6(a-b)**. Since the potential distribution on the graphene surface is related to the distribution of its carriers, the surface potential changes reflect the internal distribution of probe carriers. From the inset plot, the average potential on the R6G/3D-graphene/SOI surface is significantly higher than that of the 3D-graphene surface,

implying that the average potential will increase when an effective CT is generated between 3D-graphene, R6G molecules, and SOI substrates. These potential changes lead to a decrease in the energy difference between the Fermi energy level of 3D-graphene and the lowest unoccupied molecular orbital (LUMO) of R6G, promoting more efficient CT between 3D-graphene and R6G molecules and thus enhancing the SERS effect.[48] In addition, photocurrent mapping experiments were performed on the R6G/3D-graphene/SOI heterojunction using C-AFM under dark and light conditions, demonstrating that the photocurrent generated in the dark environment (**Fig. 6(c)**) is significantly smaller than that generated during the light illumination (**Fig. 6(d)**). More specific current value changes can be obtained in the corresponding spatial current distribution contours, as shown in **Figs. 6(e-f)**. This indicates rapid separation and transfer of light-generated charge carriers between the 3D-graphene, R6G molecules, and SOI, demonstrating that the CM contributes significantly to the enhanced SERS effect.

EB was selected as the detection molecule to verify the application of 3D-graphene/SOI heterojunction-based SERS in practical food safety. EB is a harmful food coloring additive commonly used to color foods such as beverages, seasoning, and candy. Long-term consumption of foods containing EB can easily cause adverse symptoms such as hyperactivity, emotional instability, and inability to concentrate. **Fig. 7(a)** displays the measurement setup for SERS detection of EB in the actual analysis. The appearance of the 532 nm laser irradiated on the sample is shown in **Fig. 7(b)**, where the inset is a fruity drink containing EB. **Fig. 7(c)** shows that the characteristic

Raman peaks of EB are located at 1605, 1492, 1344, 1305, and 1269 cm^{-1}, respectively, and the detection limit is as low as 10^{-9} M. Linear fitting of two characteristic peak intensities of EB, as shown in **Fig. 7(d)**, R^2 values reached around 0.983 and 0.985, respectively, proving the quantitative detection ability of EB molecules. Furthermore, the 3D-graphene/SOI heterojunction-based SERS exhibits good reproducibility. **Fig. 7(e)** shows the characteristic peaks of 10^{-6} M EB cycled 6 times, and it is observed that the results after cycling are almost the same. To study the long-term stability of the prepared SERS substrate, as exhibited in **Fig. 7(f)**, the characteristic peaks of EB can still be detected after 30 days of storage, indicating that the intensity of the characteristic peaks does not change significantly with time. Similar experiments using carmine have shown that SERS substrates also has detection limits as low as 10^{-8} M for this substance (the corresponding Raman spectra of carmine on 3D-graphene/SOI are presented in **Fig. S4**). These results further validate the practical application potential of the proposed 3D-graphene/SOI heterojunction substrate in food safety. Meanwhile, the 3D-graphene/SOI substrate was also compared with other reported ones for carmine and EB detection, as shown in **Table S2 and Table S3**. The results show good SERS sensitivity, indicating the excellent accuracy and great potential of the SERS sensor for clinical applications.

4. Conclusions

In summary, novel SERS substrates based on the 3D-graphene/SOI heterojunction were demonstrated using a simple PACVD method to detect multiple analytes

simultaneously. The novel nanocavity structure of 3D-graphene combined with the optical cavity of SOI improved interactions between 3D-graphene and incident light, a model for doubly-reinforced Raman scattering. These properties enhance electronic interactions between 3D-graphene, target molecules, and SOI substrates, improving chemical/charge transfer effects in heterojunctions. The minimum detection limits of R6G, RB, and CRV were found to be approximately 10^{-10}, 10^{-10}, and 10^{-8}, respectively. The 3D-graphene/SOI heterojunction-based SERS substrates exhibit excellent overall versatility, sensitivity, homogeneity, uniformity, stability, and reusability. In addition, EB and carmine as a food safety detection target has a detection limit as low as 10^{-9} M and 10^{-8} M. This work provides a facile fabrication method for 3D-graphene/SOI heterojunction-based SERS substrates. We hope many practical sensing applications could become possible in the near future.

Author Contributions

G. W. and Y. W. conceived the project. S. Y. and G. W. carried out theoretical research. S. Z., G. Z., Z. H., Z. L. and X. F. designed and performed the experiments. S. Z., G. W. and S. Y. performed the data analysis. Y. W., G. D. contributed to the discussion. S. Z., G. W. prepared the figures. S. Z., G. W. and Y. W. co-wrote the paper. All authors discussed the results and commented on the manuscript.

Acknowledgments

This work was supported by the National Natural Science Foundation of China under Grant (No. 62174093), and the Natural Science Foundation of Ningbo under Grant (No. 202003N4097). Y. Q. Wang acknowledges the support from the Center for Integrated Nanotechnologies (CINT), an Office of Science User Facility operated by the U. S. Department of Energy (DOE) Office of Science. Los Alamos National Laboratory, an affirmative action-equal opportunity employer, is managed by Triad National Security, LLC for the U. S. Department of Energy's NNSA, under contract 89233218CNA000001. The authors declare no competing financial interest.

Conflicts of interest

The authors declare no competing financial interests.

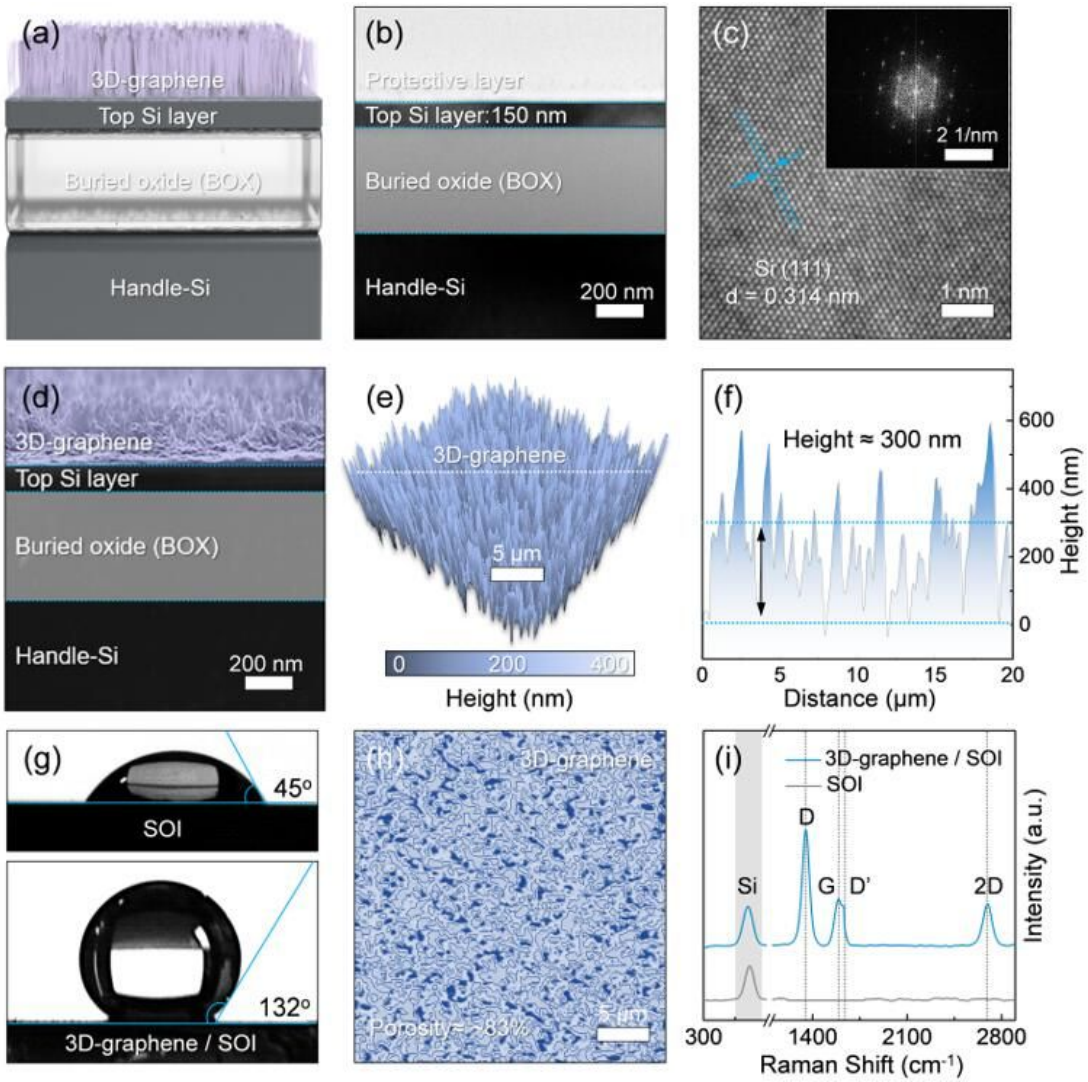

Fig. 1 Characterization of 3D-graphene on SOI substrate. (a) Arrangement of the layers in 3D-graphene/SOI heterojunction. (b) TEM image of the SOI. (c) HR-TEM image of the top Si layer (inset corresponds to FFT image). (d) Cross-sectional TEM image of 3D-graphene/SOI heterojunction. (e) 3D topographic AFM image of the 3D-graphene/SOI heterojunction. (f) Height of 3D-graphene along the white dotted line shown in (e). (g) Waterdrop images high-light the hydrophobic nature of the 3D-graphene surface. (h) Porosity plot of the 3D-graphene. (i) Raman scattering spectra of SOI and 3D-graphene/SOI.

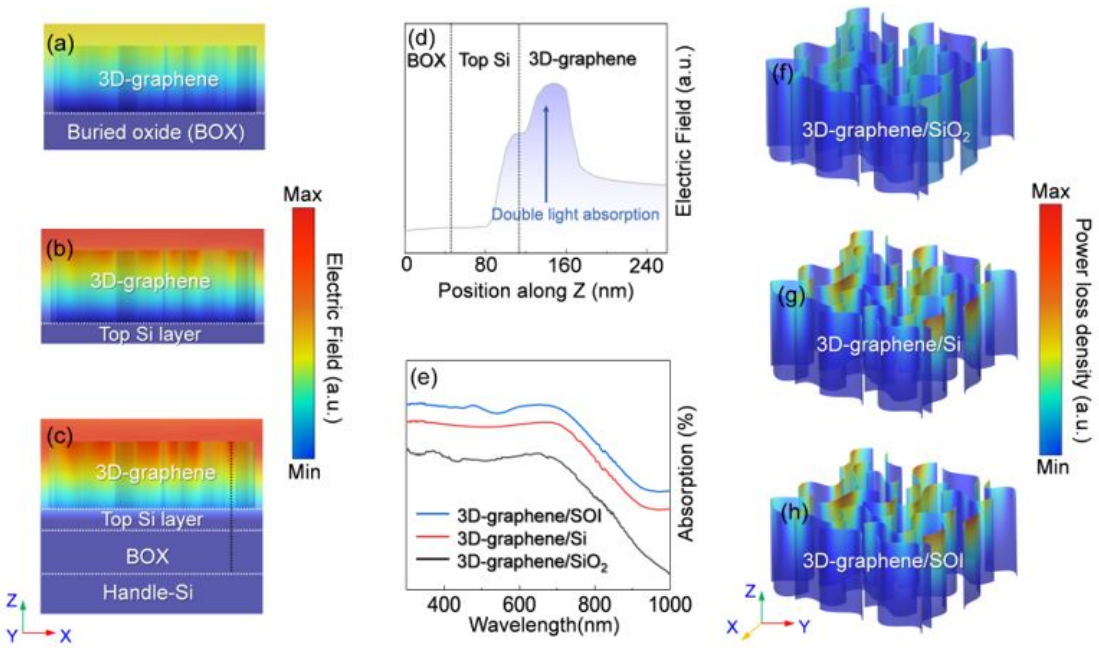

Fig. 2 The finite-element method simulations of the local electric field distribution and power loss density distribution of 3D-graphene/SOI. The finite-element method simulations of local electric field distribution of 3D-graphene on the (a) SiO_2, (b) Si, and (c) SOI substrates subjected to 532 nm laser excitation. (d) Electric field profile along the dotted vertical line is shown in (c). (e) The optical absorption spectra of 3D-graphene/SiO_2 (black line), 3D-graphene/Si (red line) and 3D-graphene/SOI (blue line). The 3D distribution perspective view of the normalized power loss density spatial distribution of (f) 3D-graphene/SiO_2, (g) 3D-graphene/Si and (h) 3D-graphene/SOI.

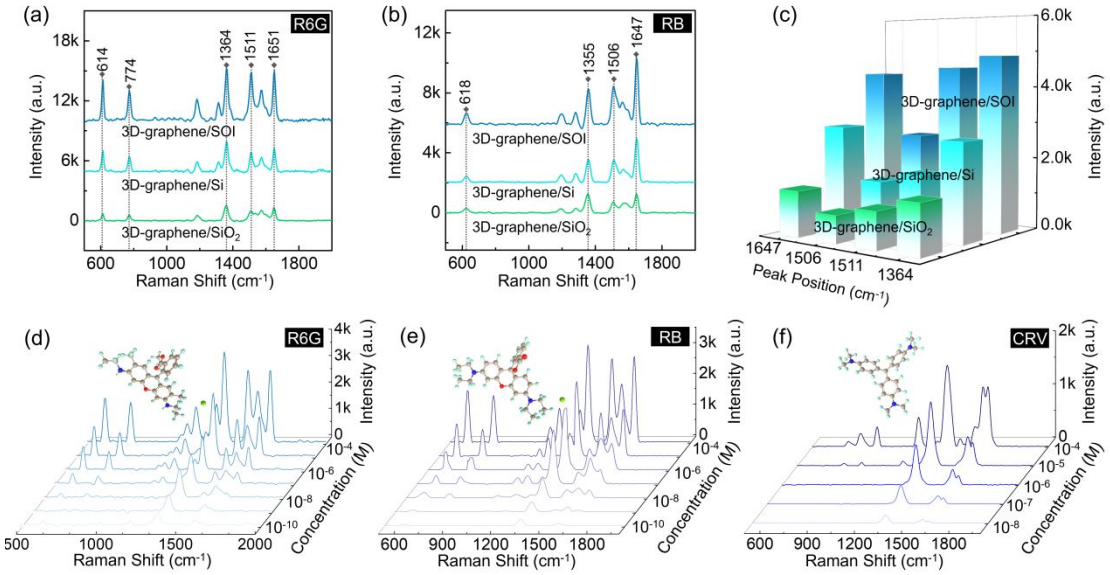

Fig. 3 Comparison of various SERS substrates. (a-b) SERS spectra of R6G and RB as probes on 3D-graphene/SiO_2, and 3D-graphene/Si, 3D-graphene/SOI. (c) A statistical plot of characteristic peak intensities of R6G and RB increasing with substrates. (The changes in the order of 3D-graphene/SiO_2, 3D-graphene/Si, 3D-graphene/SOI) (d-f) SERS spectra of R6G, RB and CRV at different concentrations. The insets represent R6G, RB, and CRV molecular structures, respectively.

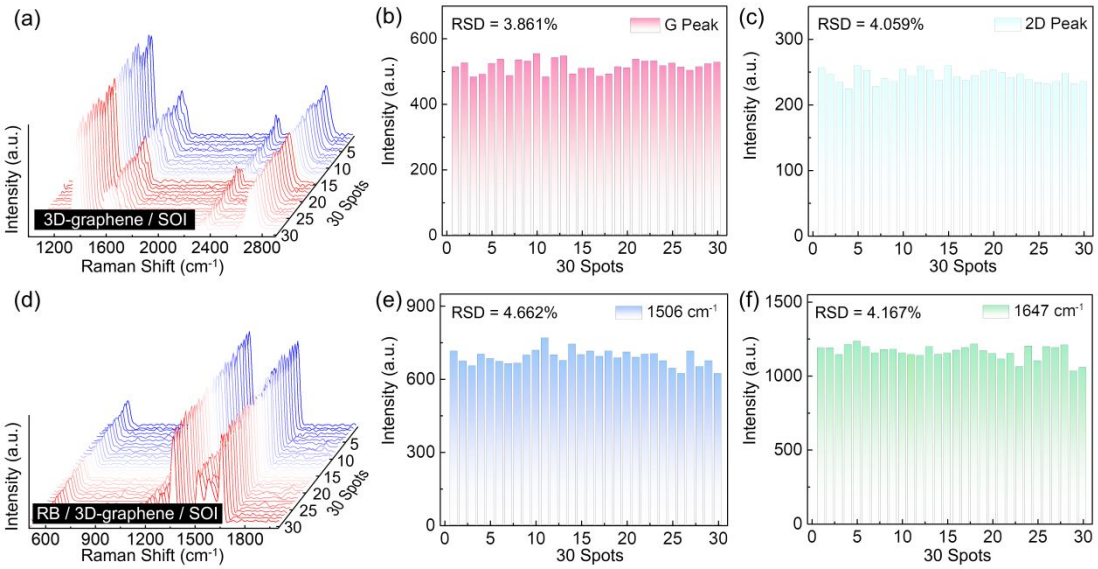

Fig. 4 Uniformity of 3D-graphene/SOI-based SERS. (a) Raman spectra were randomly collected at 30 points in a 3D-graphene/SOI heterojunction. (b-c) Raman intensity distribution of the 30 points G-peak and 2D-peak on a 3D-graphene/SOI heterojunction. (d) SERS spectra were randomly tested from 30 spots on a 3D-graphene/SOI heterojunction of 10^{-6} M RB. (e-f) Raman intensities of peaks at 1506 and 1647 cm^{-1} in 30 spectra are shown in (d).

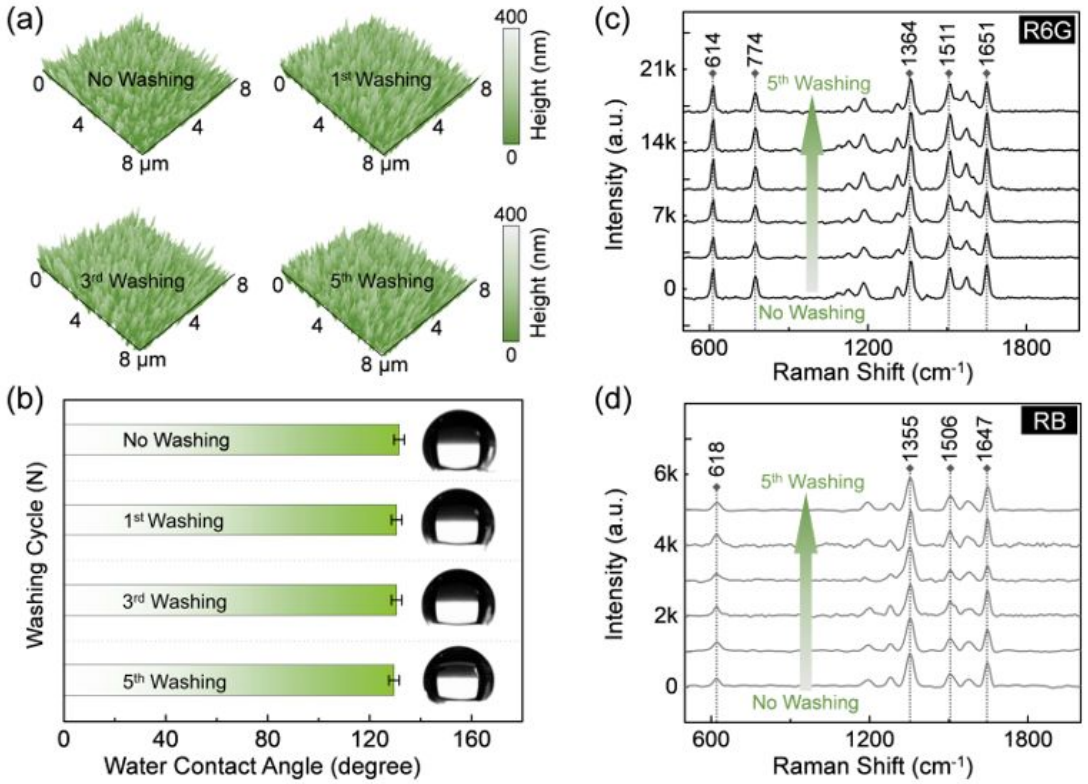

Fig. 5 Reusability of 3D-graphene/SOI-based SERS. (a) The AFM images of 3D-graphene during five ethanol washing cycles confirm the reusability of 3D-graphene/SOI as a SERS substrate. (b) The water contact angle of 3D-graphene during ethanol washing cycles. (c-d) SERS spectra of R6G and RB (concentration of 10^{-6} M) on 3D-graphene/SOI substrate during the ethanol washing.

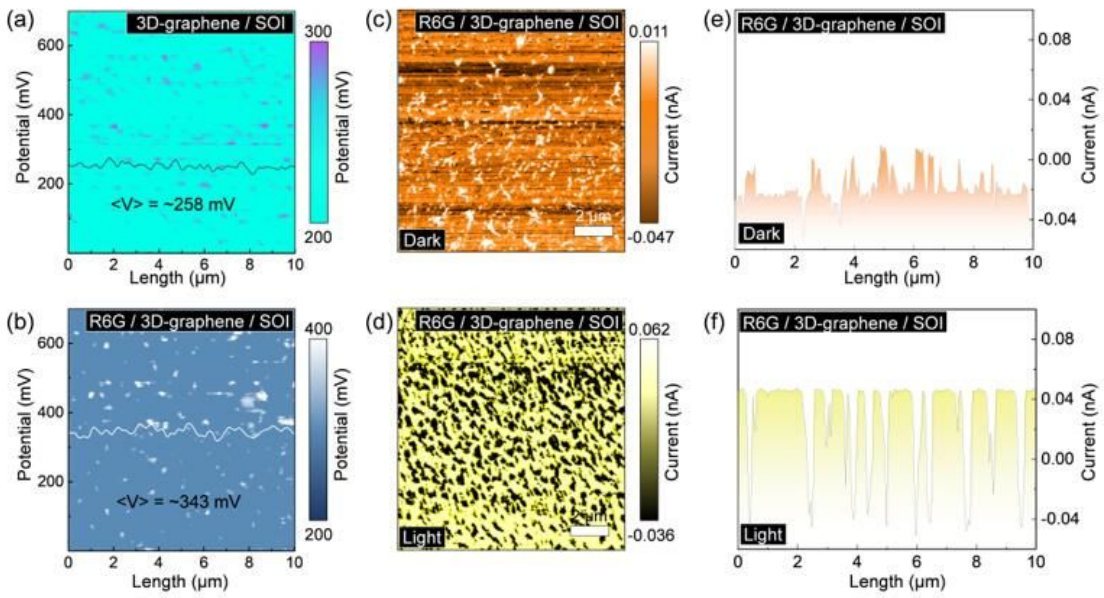

Fig. 6 Investigation of the detection mechanism of 3D-graphene/SOI-based SERS. (a-b) Surface electric potential distributions were measured on 3D-graphene/SOI and R6G/3D-graphene/SOI surfaces (concentration of 10^{-6} M). (c-d) Current plots measured using R6G (concentration of 10^{-6} M) drops over 3D-graphene/SOI heterojunction under dark and light conditions. (e-f) The corresponding current distributions in (c-d) are plotted.

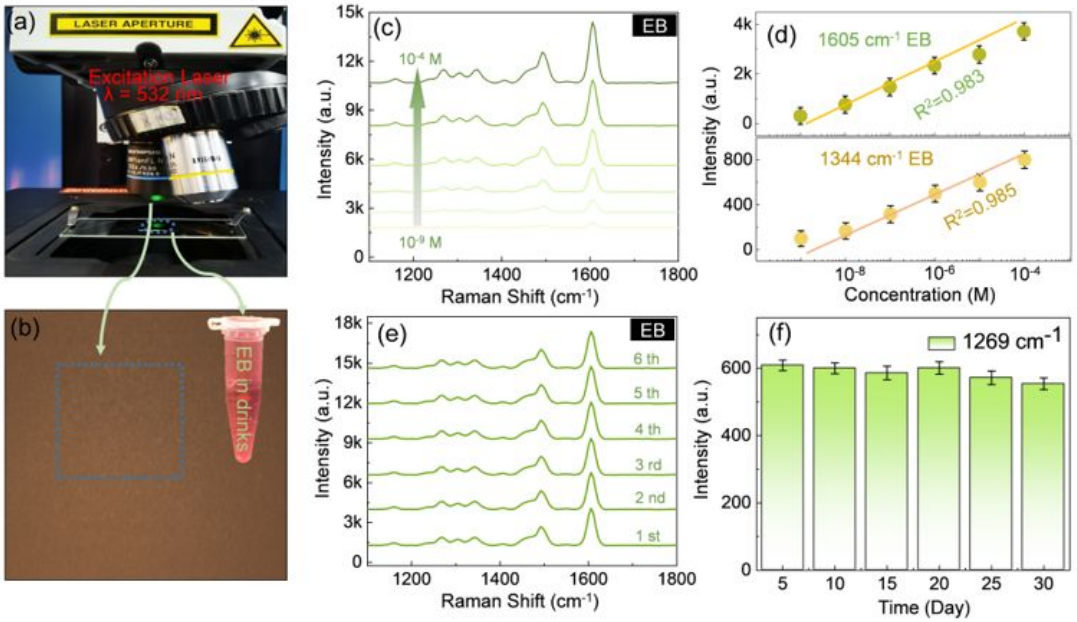

Fig. 7 Application of 3D-graphene/SOI-based SERS in food safety. (a) Photograph of the SERS measurement instrument. (b) Microscopic images of EB/3D-graphene/SOI. The inset indicates the solution to be measured. (c) SERS spectra of EB in drinks with different concentrations. (d) The logarithmic curve of 1605 and 1344 cm^{-1} of EB versus concentration. (e) SERS spectra of EB (concentration of 10^{-6} M) on 3D-graphene/SOI substrate after the ethanol washing. (f) Long-term stability of the EB spectra recorded on 3D-graphene/SOI SERS substrate.

References

1 N. Choi, H. Dang, A. Das, M. S. Sim, I. Y. Chung and J. Choo, *Biosens. Bioelectron.*, 2020, **164**, 112326.

2 J. H. Choi, W. A. El-Said and J. W. Choi, *Appl. Surf. Sci.*, 2020, **506**, 144669.

3 Y. Chang, C. Hu, R. Yang, D. He, X. Wang, B. Ning, H. Sun, Y. Xiong, J. Tu and C. Sun, *Carbohydr. Polym.*, 2020, **244**, 116460.

4 A. D` Agostino, A. M. Giovannozzi, L. Mandrile, A. Sacco, A. M. Rossi and A. Taglietti, *Talanta*, 2020, **216**, 120936.

5 L. Mandrile, I. Cagnasso, L. Berta, A. M. Giovannozzi, M. Petrozziello, F. Pellegrino, A. Asproudi, F. Durbiano and A. M. Rossi, *Food Chem.*, 2020, **326**, 127009.

6 Y. Fang, N. -H. Seong and D. D. Dlott, *Science*, 2008, **21**, 388-392.

7 L. Tao, K. Chen, Z. Chen, C. Cong, C. Qiu, J. Chen, X. Wang, H. Chen, T. Yu, W. Xie, S. Deng and J.-B. *Xu, J. Am. Chem. Soc.*, 2018, **140**, 8696-8704.

8 L. Yang, J.-H. Lee, C. Rathnam, Y. Hou, J.-W. Choi and K.-B. Lee, *Nano Lett.*, 2019, **19**, 8138-8148.

9 J. Jin, W. Song, J. Wang, L. Li, Y. Tian, S. Zhu, Y. Zhang, S. Xu, B. Yang and B. Zhao, *Chem. Eng. J.*, 2022, **430**, 132687.

10 X. Zhao, J. Dong, E. Cao, Q. Han, W. Gao, Y. Wang, J. Qi and M. Sun, *Appl. Mater. Today*, 2019, **14**, 166-174.

11 R. Das, S. Parveen, A. Bora and P. K. Giri, *Carbon*, 2020, **30**, 273-286.

12 Q. Wang, M. Chen, J. Zhang, T. Yu, F. Fu and Y. Dong, *Carbon*, 2020, **170**, 270-276.

13 M. Chen, D. Liu, X. Du, K. H. Lo, S. Wang, B. Zhou and H. Pan, *Trends. Anal. Chem.*, 2020, **130**, No. 115983.

14 N. Zhang, L. Tong and J. Zhang, *Chem. Mater.*, 2016, **28**, 6426-6435.

15 X. Ling, L. Xie, Y. Fang, H. Xu, H. Zhang, J. Kong, M. S. Dresselhaus, J. Zhang and Z. Liu, *Nano Lett.*, 2010, **10**, 553-561.

16 X. Ling, S. Huang, S. Deng, N. Mao, J. Kong, M. S. Dresselhaus and J. Zhang, *Acc. Chem. Res.*, 2015, **48**, 1862-1870.

17 D. Liu, X. Chen, Y. Hu, T. Sun, Z. Song, Y. Zheng, Y. Cao, Z. Cai, M. Cao, L. Peng, Y. Huang, L. Du, W. Yang, G. Chen, D. Wei, A. T. S. Wee and D. Wei, *Nat. Commun.*, 2018, **9**, No. 193.

18 T. Yan, L. Zhang, T. Jiang, Z. Bai, X. Yu, P. Dai and M. Wu, *Appl. Surf. Sci.*, 2017, **419**, 373-381.

19 H. Lai, F. Xu, Y. Zhang and L. Wang, *J. Mater. Chem. B*, 2018, **6**, 4008-4028.

20 F. Xu, S. Xie, R. Cao, Y. Feng, C. Ren and L. Wang, *Sens. Actuators B Chem.*, 2017, **243**, 609-616.

21 G. Ding, S. Xie, Y. Zhu, Y. Liu, L. Wang and F. Xu, *Sens. Actuators B Chem.*, 2015, **221**, 1084-1093.

22 R. Lv, M. C. Dos Santos, C. Antonelli, S. Feng, K. Fujisawa, A. Berkdemir, R. Cruz-Silva, A. L. Elías, N. Perea-Lopez, F. López-Urías, H. Terrones and M. Terrones, *Adv. Mater.*, 2014, **26**, 7593-7599.

23 Y. Cai, J. Qin, W. Li, A. Tyagi, Z. Liu, M. D. Hossain, H. Chen, J.-K. Kim, H. Liu, M. Zhuang, J. You, F. Xu, X. Lu, D. Sun, and Z. Luo, *J. Mater. Chem. A*, 2019, **7,**

27099-27109.

24 S. Huang, L. A. Panes-Ruiz, A. Croy, M. Löffler, V. Khavrus, V. Bezugly and G. Cuniberti, *Carbon*, 2021, **173**, 262-270.

25 X. Jia, M. Hu, K. Soundarapandian, X. Yu, Z. Liu, Z. Chen, A. Narita, K. Müllen, J. Jiang, K. -J. Tielrooij, M. Bonn and H. I. Wang, *Nano Lett.*, 2019, **19**, 9029-9036.

26 J. Ding, H. Zhao, Q. Wang, H. Dou, H. Chen and H. Yu, *Nanoscale*, 2017, **9**, 16871-16878.

27 M. Furchi, A. Urich, A. Pospischil, G. Lilley, K. Unterrainer, H. Detz, P. Klang, A. M. Andrews, W. Schrenk, G. Strasser and T. Mueller, *Nano Lett.*, 2012, **12**, 2773-2777.

28 D. J. Hsu, Y. Chi, K. Huang and C. Hu, *Electrochim. Acta*, 2019, **300**, 324-332.

29 P. K. Roy, A. Ganguly, W. Yang, C. Wu, J. S. Hwang, Y. Tai, K. Chen, L. Chen and S. Chattopadhyay, *Biosens. Bioelectron.*, 2015, **70**, 137-144.

30 H. Qiao, H. Liu, Z. Huang, R. Hu, Q. Ma, J. Zhong and X. Qi, *Energy Environ. Mater.*, 2021, **4**, 522-543.

31 Z. Wu, X. Zhang, L. Deng, Y. Zhang, Z. Wang, Y. Shen and G. Shao, *Energy Environ. Mater.*, 2022, **5**, 285-294.

32 P. Kuang, M. Sayed, J. Fan, B. Cheng and J. Yu, *Adv. Energy Mater.*, 2020, **10**, 1903802.

33 P. K. Roy, G. Haider, T. Chou, K. Chen, L. Chen, Y. Chen and C. Liang, *ACS Sens.*, 2019, **4**, 406-412.

34 S. Evlashin, S. Svyakhovskiy, N. Suetin, A. Pilevsky, T. Murzina, N. Novikova, A. Stepanov, A. Egorov and A. Rakhimov, *Carbon*, 2014, **70**, 111-118.

35 L. Wind, R. Böckle, M. Sistani, P. Schweizer, X. Maeder, J. Michler, C.G.E. Murphey, J. Cahoon and W.M. Weber, *ACS Appl. Mater. Interfaces*, 2022, **14**, 26238-26244.

36 Z. Cheng, R. Cao, K. Wei, Y. Yao, X. Liu, J. Kang, J. Dong, Z. Shi, H. Zhang, X. Zhang, H. Zhang and X. Zhang, *Adv. Sci.*, 2021, **8**, 2003834.

37 R.P. Srivastava and D-Y. Khang, *Adv. Mater.*, 2021, **33**, 2005932.

38 X. Zhu, L. Shi, M. S. Schmidt, A. Boisen, O. Hansen, J. Zi, S. Xiao and N. A. Mortensen, *Nano Lett.*, 2013, **13**, 4690-4696.

39 O. M. Bakr, B. H. Wunsch and F. Stellacci, *Chem. Mater.*, 2006, **18**, 3297-3301.

40 J. Guo, C. Ding, W. Gan, P. Chen, M. Zhang and Z. Sun, *J. Alloys Compd.*, 2022, **918**, 165621.

41 S.E.J. Bell, G. Charron, E. Cortés, J. Kneipp, M. L. de la Chapelle, J. Langer, M. Procházka, V. Tran and S. Schlücker, *Angew. Chem. Int. Ed.*, 2020, **59**, 5454-5462.

42 T. Szymborski, Y. Stepanenko, K. Niciński, P. Piecyk, S. M. Berus, M. Adamczyk-Popławska and A. Kamińska, *J. Mater. Res. Technol.*, 2021, **12**, 1496-1507.

43 C. Xiao, Z. Chen, M. Qin, D. Zhang and H. Wu, *Appl. Phys. Lett.*, 2018, **113**, 171604.

44 Z. Cao, P. He, T. Huang, S. Yang, S. Han, X. Wang and G. Ding, *Chem. Mater.*, 2020, **32**, 3813-3822.

45 Y. Wang, J. Liu, Y. Ozaki, Z. Xu and B. Zhao, *Chem. Int. Edit.*, 2019, **58**, 8172-8176.

46 L. Yang, W. Wang, H. Jiang, Q. Zhang, H. Shan, M. Zhang, K. Zhu, J. Lv, G. He and Z. Sun, *Sens. Actuators B Chem.*, 2017, **242**, 932-939.

47 X. Ling and J. Zhang, *Small*, 2010, **6**, 2020-2025.

48 L. Qu, Y. Liu, M. Liu, G. Yang, D. Li and H. Li, *ACS Appl. Mater. Interfaces*, 2016, **8**, 28180-28186.